Statistical features of 21 cm emission from the epoch between reionization and Gunn-Peterson transparency

Ping He[1,2], Jiren Liu[3], Long-Long Feng[4,1], Hong-Guang Bi[2], and Li-Zhi Fang[2]

ABSTRACT

We investigate the 21 cm emission from the epoch between reionization z_r and the Gunn-Peterson transparency z_{GP}. According to the lognormal model of the thermal history around reionization, hydrogen clouds in $z_r > z > z_{GP}$ are hot and a predominant part of baryonic gas is ionized, but still opaque to Lyα photons. Therefore, 21 cm emission is a distinctive characteristic of this epoch. We show that the 21 cm emission comes from both uncollapsed and collapsing hydrogen clouds. The spatial distribution of the brightness temperature excess δT_b is highly non-Gaussian. It consists of spikes with high δT_b and a low δT_b area between the spikes. The field has the following statistical features: (1) the one-point distributions of δT_b are described approximately by power-law tailed probability distribution functions; (2) the nth-order moment of δT_b is increasing much faster with n than that of a Gaussian field, but slower than that of a lognormal field; (3) the scale-scale correlation of δT_b field is significant for all scales larger than the Jeans length of the gas. These features would be useful for distinguishing the 21 cm emission of the early clustering from the noise of foreground contamination.

Subject headings: cosmology: theory – intergalactic medium – large-scale structure of the universe

1. Introduction

The universe becomes transparent to Lyα photons (the Gunn-Peterson transparency) at redshift $z_{GP} \simeq 6.5$ (Fan et al. 2002). Yet the polarization of the cosmic microwave

[1]National Astronomical Observatories, Chinese Academy of Sciences, 20A Datun Road, Chaoyang, Beijing 100012, China

[2]Department of Physics, University of Arizona, Tucson, AZ 85721

[3]Center for Astrophysics, University of Science and Technology of China, Hefei 230026, China

[4]Purple Mountain Observatory, Nanjing 210008, China

background (CMB) indicates that the Compton scattering optical depth to the CMB is as high as $\tau_e \simeq 0.17 \pm 0.04$ and that the reionization of the universe probably occurred at $11 < z_r < 30$ (Kogut et al. 2003). Most theoretical attempts to discriminate between the redshifts z_{GP} and z_r concluded that the history from first-generation star formation to the Gunn-Peterson transparency lasts a long time (Cen 2003; Haiman & Holder 2003; Whyithe & Loeb 2003; Holder et al. 2003; Onken & Miralda-Escudé 2003).

This problem has recently been studied by using the lognormal (LN) formalism (Bi et al. 2003; Liu et al. 2004). Considering that the Jeans length changed greatly before and after the reionization, a self-consistent calculation with the LN model yields a general picture that the redshift z_r should be significantly larger than z_{GP}, where z_r means the era that ionized regions are fully overlapped. The thermal history of the universe around the reionization can be roughly divided into three epochs: (1) the cold dark age $z > z_r$, (2) the hot dark age $z_r > z > z_{GP}$, and (3) the bright age $z < z_{GP}$. With the cosmological parameters given by WMAP and COBE, the hot dark age lasts about $z_r - z_{GP} \simeq 10$.

In the epoch $z_r > z > z_{GP}$, the fraction of ionized hydrogen $f_{HII} = n_{HII}/(n_{HI} + n_{HII})$, where n_{HI} and n_{HII} are the number densities of neutral and ionized hydrogen atoms, is already significant, while the mass fraction of neutral hydrogen $f_{HI} = n_{HI}/(n_{HI} + n_{HII})$ is still much greater than 10^{-3}, so that the universe is opaque to the Lyα photons. Moreover, the temperature of hydrogen gas in the period $z_r > z > z_{GP}$ is higher than that of the CMB. Therefore, in this epoch, the 21 cm emission given by the hyperfine structure of the ground state $1^2S_{1/2}$ of neutral hydrogen would be significant. This motivates us to investigate in this paper the statistical properties of the redshifted 21 cm emission from the epoch $z_r > z > z_{GP}$.

Many calculations on the redshifted 21 cm radiation from the early universe have been done based on various models of the thermal history around reionization (Ciardi & Madau 2003; Furlanetto & Loeb 2002, 2004; Iliev et al. 2002, 2003; Tozzi et al. 2000; Zaldarriaga et al. 2004; Furlanetto et al. 2004). These works have generally focused on the power spectrum of the fluctuations of the 21 cm emission. In this paper, besides the power spectrum, we address the higher order statistics and non-Gaussianity of the spatial distribution of the 21 cm emission. Since the 21 cm emission at high redshifts is relevant to the earliest gravitational clustering and star formation of the universe, the field of the 21 cm emission must be non-Gaussian. It would probably be the earliest non-Gaussian field if the initial perturbations of cosmic mass density field are Gaussian.

The non-Gaussianity of 21 cm emission field is not only theoretically important but also observationally useful. Radio observation would be able to detect the cosmic 21 cm emissions if its flux is of the order of $\simeq 0.1$ mJy or higher and angular scale is of the order of arcminutes (Morales and Hewitt 2004; Pen et al. 2004). However, it is a challenge to

identify the redshifted 21 cm emission from the recombination epoch, since the noise from the artificial radio interference in the VHF band is serious. The non-Gaussian statistical features would be helpful to draw the information from the noisy observations.

This paper is outlined as follows. §2 briefly describes the basic results of the reionization and thermal history of hydrogen clouds in the LN model. §3 presents the simulations of the baryon field and the 21 cm emission from neutral hydrogen in the epoch of z_r to z_{GP}. The basic properties of the 21 cm emission from diffused intergalactic medium (IGM) and collapsed halos are also addressed. §4 presents a statistical analysis of the δT_b fields, including the first-, second- and high-order statistics. Finally §5 gives the discussion and conclusion.

2. Evolution of hydrogen clouds around reionization

2.1. Hydrogen gas distribution in LN model

The LN model assumes that the mass density distribution $\rho(\mathbf{x})$ of hydrogen gas at redshift z is given by an exponential mapping of the linear distribution of the dark matter mass density contrast $\delta_0(\mathbf{x})$, which is smoothed on the Jeans length scale of the gas at the redshift z (Bi 1993), i.e.,

$$\rho(\mathbf{x}) = \bar{\rho}_0 \exp[\delta_0(\mathbf{x}) - \sigma_0^2/2], \tag{1}$$

where $\bar{\rho}_0$ is the mean density and $\sigma_0 = \langle \delta_0^2 \rangle^{1/2}$ is the variance of the Gaussian mass field $\delta_0(\mathbf{x})$ on the scale of the Jeans length of the gas. The probability distribution function (PDF) of the density field $\rho(\mathbf{x})$ is, then, lognormal:

$$p(\rho/\bar{\rho}) = \frac{1}{(\rho/\bar{\rho})\sigma_0\sqrt{2\pi}} \exp\left[-\frac{1}{2}\left(\frac{\ln(\rho/\bar{\rho}) + \sigma_0^2/2}{\sigma_0}\right)^2\right], \quad \rho \geq 0. \tag{2}$$

The dynamical arguments of the exponential mapping and LN PDF of both the dark matter and hydrogen clouds have been studied by, e.g., Coles & Jones (1991), Jones (1999), and Szapudi & Kaiser (2003).

The first characteristic of the LN model is that the clustering of hydrogen clouds is mainly dependent on the variance σ_0 of the linear fluctuations on the scale of the Jeans length, while the clustering of dark matter basically is independent of the properties of gas. Therefore, the LN model is effective in describing the effect of the thermal status of hydrogen gas on the density and velocity field of the baryonic gas. This has been shown in the successful application of modelling IGM Lyα forests of QSO's absorption spectra in redshift range $2 \leq z \leq 5$ (Bi 1993; Bi & Davidsen 1997; Feng & Fang 2000).

The second characteristic is that, compared to a Gaussian or a normal distribution, the PDF of an LN model described by equation (2) has a prolonged tail at the high-density end and that the probability of high-density events $\rho/\bar{\rho} \gg 1$ is very sensitive to σ_0. This property has already been found to be useful in explaining the intermittence of the transmitted flux of QSO's Lyα absorption spectrum (Jamkhedkar et al. 2000, 2003; Pando et al. 2002). The long tail can directly be seen with (1) the cumulative mass fraction $M(> \rho/\bar{\rho})$, which is the fraction of mass in regions having mass density larger than a given ρ, and (2) the volume filling factor $V(> \rho/\bar{\rho})$, which is the fraction of volume with density larger than a given ρ. They are

$$M[> (\rho/\bar{\rho})] = \int_{\rho/\bar{\rho}}^{\infty} xp(x)dx = \frac{1}{2}\mathrm{erfc}\left(\frac{\ln(\rho/\bar{\rho})}{\sqrt{2}\sigma_0} - \frac{\sigma_0}{2\sqrt{2}}\right), \tag{3}$$

$$V(> \rho/\bar{\rho}) = \int_{\rho/\bar{\rho}}^{\infty} p(x)dx = \frac{1}{2}\mathrm{erfc}\left(\frac{\sigma_0}{2\sqrt{2}} + \frac{\ln(\rho/\bar{\rho})}{\sqrt{2}\sigma_0}\right). \tag{4}$$

Therefore, even when $\sigma_0 \simeq 1$, the mass fraction of high-density events is already significant and their volume filling factor is very small.

2.2. The clustering of hydrogen clouds at redshifts z_r and z_{GP}

In the context of the LN model, the evolution of hydrogen clouds is mainly dependent on the Jeans length of hydrogen gas. If hydrogen gas is uniformly distributed, its Jeans length is given by $\lambda_J \equiv v_s(\pi/G\rho)^{1/2}$, where v_s is the sound speed of the gas. For cosmological study, it is convenient to use a comoving scale $x_J = \lambda_J/2\pi = (1/H_0)[2\gamma k_B T_m/3\mu m_p \Omega(1+z)]^{1/2}$, where T_m is the mean temperature, μ the molecular weight of the gas, Ω is the cosmological density parameter of total mass, and γ is the ratio of specific heat.

Primordial baryons, created at the time of nucleosynthesis, recombine with electrons to become neutral gas at $z \simeq 1000$. Before $z \simeq 200$, the residual ionization of the cosmic gas keeps its temperature locked to the CMB temperature (Peebles 1993). After $z \simeq 200$, the gas cools down adiabatically because of the expansion of the universe. Assuming the adiabatic index $\gamma = 5/3$, i.e., hydrogen temperature $T \propto \rho^{2/3}$, the comoving Jeans length evolves as $\simeq 0.1 \times (1+z)^{1/2}\ h^{-1}$ kpc. During reionization, the gas is heated by UV ionizing photons from a low temperature to $\sim 1.3 \times 10^4$K. This leads to the increase of x_J at z_r.

Assuming $z_r \simeq 18$ (Kogut et al. 2003; Liu et al. 2004), the evolution of the Jeans length is sketched in Figure 1, which gives the relation between x_J and the cosmic scale factor $1/(1+z)$. The sudden increase of x_J at z_r shown in Figure 1 is certainly unrealistic, which comes from the assumption that the gas temperature increases instantly by a factor of about 10^4 at z_r. More realistically, the sharp changes of x_J at z_r and z_{GP} should be replaced

by a softened transition. Nevertheless, the physical status of the gas before and after z_r is properly sketched in Figure 1.

Corresponding to the evolution of x_J at z_r, the variance σ_0, which is the *rms* mass fluctuation on the Jeans length $(\delta\rho/\rho)_{x_J} \propto k^3P(k)|_{k=1/x_J}$, also undergoes a zigzag evolution around z_r. Figure 2 shows σ_0 versus $1/(1+z)$ calculated with the x_J of Figure 1. To calculate σ_0, the power spectrum $P(k)$ of the linear mass density perturbations is taken to be the spectrum of the low-density flat cold dark matter model (LCDM), which is specified by the density parameter $\Omega_0 = 0.3$, the cosmological constant $\Omega_\Lambda = 0.7$, and the Hubble constant $h = 0.7$. The linear power spectrum $P(k)$ is given by the fitting formula given by Eisenstein & Hu (1999). The increase of σ_0 with $1/(1+z)$ shown in Figure 2 is due to the gravitational linear growth. The variance at small redshifts ($z < 7$) shown in Figure 2 actually is the same as that given by Bi & Davidsen (1997). The zigzagged feature at $z \simeq 3.3$ of Figure 2 is due to HeII reionization (Theuns et al. 2002).

An important feature of σ_0 shown in Figure 2 is that the curve of σ_0 from A' to B' almost repeats that from A to B. Thus, the evolution of the fraction of mass [eq.(3)] in the period from A' to B' is similar to that from A to B. The period from A to B corresponds to an evolution of weak-to-strong clustering of the baryonic gas, and the period from A' to B' also corresponds to an evolution of weak-to-strong clustering of baryonic gas. Therefore, the formation rate of collapsed hydrogen clouds at A' is significantly lower than that at B. This leads to a suppression of clustering and star formation just after z_r.

The dynamical picture of the suppression of clustering can be explained by the following negative feedback mechanism. During the reionization z_r, hydrogen clouds are heated by the ionizing photons so that the mean temperature of hydrogen clouds increases by a few orders. All the irregularities originally formed in cold gas on scales smaller than the new Jeans length would be smoothed out by the heated gas, and the variance of the fluctuations of hydrogen cloud distribution drops back below unity. Although dark matter halos continuously collapse before and after z_r, hydrogen clouds on scales less than the new Jeans length will stop collapsing. As a result, star formation will be slowed down or may be even halted in these halos after z_r. The level of the star formation suppression is adjusted by the following mechanism. Once the star formation rate declines, the UV background produced by the star formation also becomes lower, and so do the temperature and entropy states of hydrogen gas, which make it easy for further star formation. On the contrary, if the star formation rate increases, the UV background produced by the star formation also increases, and then more hydrogen gas will be heated to higher temperature and higher entropy states. This finally yields more suppression in the rate of star formation.

When the variance σ_0 grows again to unity around B' because of the increase of the

potential wells of dark matter, there is once again enough to have collapsed hydrogen clouds, star formation, and ionizing photons. This finally gives rise to the Gunn-Peterson transparency. Therefore, the long-lasting period from z_r to z_{GP} is due to the zigzag of σ_0 around reionization z_r. The difference $z_r - z_{GP}$ is found to be equal to $\simeq 10$. It is weakly dependent on, or stable with respect to, the following parameters: (1) the threshold of the collapsed hydrogen clouds $\rho/\bar{\rho}$ and (2) the mean ionizing photons released by each baryon in the collapsed objects (Liu et al. 2004). This stability is due to the above-mentioned adjustment mechanism. In this sense, the redshift of reionization $z_r \simeq 18$ actually is determined by the redshift of the Gunn-Peterson transparency z_{GP} (Liu et al. 2004). This result is also in good agreement with the observed optical depth τ_e to the CMB photons.

2.3. Temperature of hydrogen clouds in the epoch of z_r to z_{pg}

According to the above-discussed scenario, in the epoch $z > z_r$, hydrogen gas is cold and neutral. It may contain some individual ionized spheres around the first-generation stars. Hydrogen clouds generally are opaque to Lyα photons. When z approaches z_r, the increasing individual ionized regions overlap. At z_r, the individual ionized regions fully overlap in the sense that the universe becomes transparent to soft X-ray photons. Thus, after z_r, hydrogen clouds are heated by soft X-ray photons and the star formation is suppressed. The fraction of ionized hydrogen (HII) will no longer increase, or will even decrease after z_r. Consequently, hydrogen clouds are still opaque to Lyα photons.

It has been shown that if the photoionization heating is the major heating process of the hydrogen clouds, the mean gas temperature is always of the order of $\sim 10^4$ K, weakly dependent on the intensity of heating photons (Black 1981; Ostriker & Ikeuchi 1983). This result is further supported by hydrodynamic simulations of baryonic gas in the early universe (e.g., Hui & Haiman 2003). They showed that the mean gas temperature asymptotically approaches $10^3 - 10^4$ K. This temperature is not determined by the intensity of the heating photons, but is completely given by the shape (or hardness) of the spectrum of the heating photons. The mean temperature is higher for harder photon spectra, such as soft X-rays. Thus, although star formation is slowing down after z_r, the mean temperature will still be in the range $10^3 - 10^4$ K. Therefore, it is reasonable to assume that in the epoch of z_r to z_{GP}, the mean gas temperature can be described as $T_m \simeq T_0[(1+z)/(1+z_r)]^\eta$, where $T_0 \simeq 10^4$K and the index η is of the order of 1. In Figure 3, we plot the mean temperature evolution for the two cases of $(T_0, \eta) = (0.8 \times 10^4 K, 2)$ and $(1.3 \times 10^4 K, 2)$. In Figures 1 and 2 we also show, respectively, the temperature effect on the Jeans length x_J and variance σ_0 in the epoch $z_r > z > z_{GP}$.

If hydrogen gas is polytropic, gas temperature at the point with mass density ρ is given by $T = T_m(\rho/\bar{\rho})^{\gamma-1}$. In this way, we can calculate the thermal status of hydrogen from the density distribution. In the LN model, the relation $T-\rho$ and the index γ actually are given by fitting the hydrodynamical simulation (Bi & Davidsen 1997). In this case, shock heating is partially considered. However, if gravitational shocks are strong, the temperature of hydrogen gas is basically multiphased, and one cannot describe the $T-\rho$ relation by a single equation. To estimate the effect of strong shock, we have to replace the temperature-density relation $T = T_m(\rho/\bar{\rho})^{\gamma-1}$ with $P(T;\rho)$, the PDF of temperature at a given ρ. Such a PDF has been recently derived by using a hydrodynamic simulation code that is very effective in capturing shocks (He et al. 2004). He et al. (2004) found that strong shock events are very rare at $z > 4$, i.e., that the events leading to the deviation from the relation $T = T_m(\rho/\bar{\rho})^{\gamma-1}$ are negligible at $z > 4$.

3. Samples from the LN simulation

3.1. Simulation of the hydrogen gas distribution

We produce simulation samples of spatial distribution of hydrogen gas $\rho(\mathbf{x})$ by the LN model. In order to quickly grasp the features of these distributions, we only concentrate on samples of one-dimensional distribution. The details of the simulation procedures have been given in Bi & Davidsen (1997) and Bi et al. (2003). A brief description is as follows.

We first generate the one-dimensional density and velocity distributions in Fourier space, $\delta_0(k,z)$ and $v(k,z)$, which are two Gaussian random fields. Both $\delta_0(k,z)$ and $v(k,z)$ are given by the power spectrum, $P_0(k)$ as follows (Bi 1993; Bi et al. 1995)

$$\delta_0(k,z) = D(z)(u(k)+w(k)), \tag{5}$$

$$v(k,z) = F(z)\frac{H_0}{c} ik\alpha(k)w(k), \tag{6}$$

where $D(z)$ and $F(z)$ are the linear growth factors for the $\delta_0(x)$ and $v(x)$ fields at redshift z. The $w(k)$ and $u(k)$ fields are Gaussian with the power spectra given by

$$P_w(k) = \alpha^{-1}\int_k^\infty P_0(q) 2\pi q^{-1} dq, \tag{7}$$

$$P_u(k) = \int_k^\infty P_0(q) 2\pi q dq - P_w(k), \tag{8}$$

where $P_0(k)$ is the power spectrum of the three-dimensional field $\delta_0(\mathbf{x})$. The functions $\alpha(k)$ in equation (7) is defined by

$$\alpha(k) = \frac{\int_k^\infty P_0(q) q^{-3} dq}{\int_k^\infty P_0(q) q^{-1} dq}. \tag{9}$$

The power spectrum $P_0(k)$ is taken to be (Bi & Davidsen 1997; Bi et al. 2003)

$$P_0(k) = \frac{P_{dm}(k)}{(1 + x_J^2 k^2)^2}. \tag{10}$$

Obviously, $P_0(k)$ is also a function of z via the redshift dependence of $x_J(z)$. Thus, for a given $P_{DM}(k)$ and x_J, one can produce the distributions $\delta_0(k, z)$ at the grid points k_i, $i = 1, 2, ..., N$ in one-dimensional Fourier space. The spatial distributions $\delta_0(x, z)$ can be obtained by using the fast Fourier transform. Since the velocity follows the linear evolution longer than the density, we can use the linear $v(k, z)$ and its Fourier counterpart as good approximations of the velocity field at high redshifts. In Figure 4 we plot a typical realization of the gas mass density fields at redshifts 7, 10, and 15. The simulation size shown in Figure 4 is 50 h^{-1} Mpc in comoving space. The total number of pixels is $2^{14} = 16,384$. The pixel size is then $\simeq 3$ h^{-1} kpc, which is less than the smallest scale of x_J at $z < z_r$. Therefore, the samples are qualified for studying the non-Gaussian features of the hydrogen clouds on small scales.

As analyzed in §2.3, the effect of strong gravitational shock at high redshifts is negligible and the temperature of hydrogen gas can be calculated by the relation $T = T_m(\rho/\bar{\rho})^{\gamma-1}$. We then have the temperature field of the hydrogen clouds. With the mass density and temperature fields, one can find the neutral hydrogen mass density fields with the photoionization equilibrium equation as

$$f_{HI} = \frac{\alpha(T)}{\alpha(T) + \Gamma(T) + J/n_e}, \tag{11}$$

where $\alpha(T)$ is the recombination rate, $\Gamma(T)$ is the collisional ionization rate, n_e is the number density of electrons, and J the rate of photoionization of hydrogen (Black 1981). Although equation (11) is reasonable for determining f_{HI} of the IGM at $z < z_{GP}$, there are two points should be addressed when applying it to the epoch $z_r - z_{GP}$.

First, equation (11) is applicable only if the hydrogen clouds are optically thin for photons of J. However, hydrogen clouds of $z_r > z > z_{GP}$ are optically thick for Lyα photons and may also be so for photons of ~ 13.6 eV. Therefore, in our case, the flux J in equation (11) is not for Lyα, but for soft X-ray photons. As discussed in §2.3, in the epoch $z_r > z > z_{GP}$, hydrogen clouds are transparent to soft X-ray photons, which are the major sources of photoionization heating. This picture is consistent with the fact that the photon spectra from the first-generation (massive) stars are generally hard.

Second, in the case of $z < z_{GP}$, the parameter J is determined by fitting it with the mean transmitted flux of Lyα photons (e.g., Choudhury et al. 2001). Obviously, no such observations can be used to constrain the parameter J in the epoch of $z_r > z > z_{GP}$. However, J/n_e can be adjusted by fitting it to the mean fractions of HI or HII, which are required by the optical depth τ_e. Using this method, we can produce samples of f_{HI} field. Both the models of (T_0, η)=$(0.8\times 10^4 K, 2)$ and $(1.3\times 10^4 K, 2)$ are consistent with the optical depth τ_e from the WMAP.

3.2. Simulation of the 21 cm emission of hydrogen clouds

With the sample of gas mass density, temperature, and f_{HI} distributions, we can calculate the 21 cm ($\nu_0 = 1420$ MHz) emission of neutral hydrogen (HI). This emission at redshift z is determined by the difference between the spin temperature of neutral hydrogen, $T_s(z)$, and the temperature of the cosmic microwave background, $T_{CMB}(z) = 2.73(1+z)$ K. There are two mechanisms leading to $T_s(z) > T_{CMB}$, collision and radiation background, which gives (Field 1958, 1959)

$$T_s = \frac{T_{CMB} + y_c T_c + y_L T_L}{1 + y_c + y_L}, \tag{12}$$

where T_c is the temperature of hydrogen gas, T_L is the temperature of Lyα photons, and y_c and y_L are the collision and radiative excitation efficiencies, respectively. Since hydrogen clouds are optically thick to the Lyα photons, it is reasonable to assume that Lyα photons are in approximate thermal equilibrium with the gas. Thus, one can take T_L to be the gas temperature.

Considering self-absorption, the brightness temperature of the 21 cm radiation at redshift z is determined from the radiation transfer equation as

$$T_b(z) = T_{cmb}(z) e^{-\tau(z)} + \int_0^{\tau(z)} T_s(z') e^{-\tau(z')} d\tau(z'), \tag{13}$$

where the first term on the right-hand side is from the CMB and the second term is from neutral hydrogen; $\tau(z)$ is the optical depth of the 21 cm absorption. When T_s is much larger than $T_* = h\nu_0/k_B = 0.06$ K, $\tau(z)$ is given by (Wild 1952)

$$\tau(z) = \frac{3hc^3 A_{10}}{32\pi\nu_0^2 k_B} \int_0^{z_r} \frac{n_{HI}(z')}{T_s(z')H(z')} F(z, z') dz', \tag{14}$$

where factor $F(z, z')$ is the normalized line profile. For Doppler broadening, we have

$$F(z, z') = \frac{1}{\sqrt{\pi} b(1+z)} e^{-\left(\frac{z'-z}{b(1+z)}\right)^2}, \tag{15}$$

where $b = (2k_BT/mc^2)^{1/2}$. For gas with temperature $\leq 10^5$ K, we have $b \leq 10^{-4}$, and therefore the integral of equation (14) lasts for a very narrow range $z \pm \Delta z$ and $\Delta z \leq 10^{-4}(1+z)$. Thus, the velocity distortion can be ignored in the first stage.

If $n_{HI}(z)$ and $T_s(z)$ are not strong functions of z, equation (14) gives approximately (Field 1959)

$$\tau(z) = \frac{3hc^3 A_{10} n_{HI}(z)}{32\pi\nu_0^2 k_B T_s(z) H(z)}. \tag{16}$$

Therefore the fields $n_{HI}(z)$ and $T_s(z)$ in equation (16) are, respectively, the HI number density and spin temperature $T_s(z)$ smoothed by the window function equation (15). Thus, equation (13) yields approximately $T_b(z) = T_{CMB}(z)e^{-\tau(z)} + T_s(z)(1 - e^{-\tau(z)})$, and therefore the observed brightness temperature excess at the redshifted frequency $\nu = \nu_0/(1+z)$ is

$$\delta T_b(\nu) = [T_s(z) - T_{cmb}(z)]\frac{1 - e^{-\tau(z)}}{1+z}. \tag{17}$$

We show in Figure 5 a typical realization of the fields of T_b, $\tau(z)$, and δT_b at z=7 in the temperature model $(T_0, \eta) = (1.3 \times 10^4 K, 2)$. Figure 5 shows that the field of the brightness temperature excess, δT_b, is highly nonuniform. At most places, δT_b is actually zero but contains many high spikes, or patchy structures. The average of δT_b is only $\simeq 2.3mK$, while the spikes can be as high as 20 - 40 mK. The rms of the brightness temperature fluctuations, $\langle \delta T_b^2 \rangle^{1/2}$, is $\simeq$ 7 mK. For $(T_0, \eta) = (0.8 \times 10^4 K, 2)$, we have $\langle \delta T_b^2 \rangle^{1/2} = 9.5$ mK. It has been argued that the brightness temperature excess would be too small to observe when considering the foreground noise contamination. However, the nontrivial features of the non-Gaussianity might help identify the redshifted 21 cm emission from the contaminated data.

The non-Gaussianity of the δT_b field can also be seen with $(d\langle \delta T_b^2 \rangle^{1/2}/d\rho)d\rho$, which is the fraction of $\langle \delta T_b^2 \rangle^{1/2}$ given by regions with hydrogen gas density from ρ to ρ+$d\rho$. Figure 6 plots the integrated fraction function $\langle \delta T_b^2 \rangle^{1/2}(> \rho) = \int_\rho^\infty d\langle \delta T_b^2 \rangle^{1/2}$. It shows that about one-third of $\langle \delta T_b^2 \rangle^{1/2}$ is given by regions with density $2 < \rho < 6$ and that the other two-thirds are from regions of $\rho \geq 6$. Because the $\rho \geq 6$ regions correspond to the collapsed/collapsing hydrogen clouds (Bi et al. 2003; Liu et al. 2004), Figure 6 shows that both diffused and collapsed hydrogen clouds of the mass field have comparable contributions to the brightness temperature fluctuations of the redshifted 21 cm emission. Therefore, the non-Gaussianity caused by the quasi-linear and the nonlinear clustering of hydrogen clouds should be significant.

4. Statistical properties of 21-cm emissions

4.1. DWT variables of δT_b field

In order to effectively describe statistical features of δT_b field, we decompose the δT_b field by the discrete wavelet transform (DWT; Fang & Feng 2000; Fang & Thews 1998). Because the DWT modes are spatially localized, each dimension can be treated separately, and hence it is easy to match the simulation with the physical condition of the sampling. The three-dimensional power spectrum can be effectively recovered by DWT from the data in an area with "poor" geometry. Therefore, with the DWT, one can effectively compare and test the predicted statistical properties from one-dimensional or two-dimensional simulation with various observations (e.g., Guo et al. 2004 and references therein).

In the DWT scheme, there are two sets of bases given by (1) scaling functions $\phi_{j,l}(x) = \langle x|j,l\rangle_s$ and (2) wavelets $\psi_{j,l}(x) = \langle x|j,l\rangle_w$, where $j = 0, 1, ..$ and $l = 0, 1...2^j - 1$. In one-dimensional space with size L, the scaling function $\phi_{j,l}(x)$ is localized in physical space $lL/2^j < x \leq (l+1)L/2^j$ while wavelet $\psi_{j,l}$ is localized in both physical space $lL/2^j < x \leq (l+1)L/2^j$ and Fourier space $\pi 2^j/L < |k| < (3/2)2\pi 2^j/L$.

The scaling functions are orthonormal with respect to the index l as

$$_s\langle j,l|j,l'\rangle_s \equiv \int \phi_{j,l}(\mathbf{x})\phi_{j,l'}(\mathbf{x})dx = \delta^K_{l,l'}. \tag{18}$$

Scaling function $\phi_{j,l}(x)$ actually is a window function for the spatial range $lL/2^j < x \leq (l+1)L/2^j$. The scaling function coefficient (SFC) of a field $\delta T_b(x)$ is defined as $\epsilon_{j,l} \equiv {}_s\langle j,l|\delta T_b\rangle = \int \delta T_b(x)\phi_{j,l}(x)dx$, and therefore, the mean of $\delta T_b(x)$ in the spatial range $lL/2^j < x \leq (l+1)L/2^j$ is

$$\delta T_{b,(j,l)} = \frac{\epsilon_{j,l}}{_s\langle j,l|1\rangle}, \tag{19}$$

where $|1\rangle$ is a uniform field with field strength equal to unity.

The wavelets $\psi_{j,l}(x)$ are orthonormal bases with respect to both indexes j and l

$$_s\langle j,l|j',l'\rangle_s \equiv \int \psi_{j,l}(x)\psi_{j',l'}(x)dx = \delta_{j,j'}\delta_{l,l'}. \tag{20}$$

The wavelet function coefficient (WFC) of the $\delta T_b(x)$ field is defined as

$$\tilde{\epsilon}_{j,l} \equiv {}_w\langle j,l|\delta\rangle = \int \delta T_b(x)\psi_{j,l}(x)dx. \tag{21}$$

Since the set of the wavelet bases $|j,l\rangle_w$ is complete, the $\delta T_b(x)$ field can be expressed as

$$\delta T_b(x) = \sum_j \sum_l \tilde{\epsilon}_{j,l}\psi_{j,l}(x), \tag{22}$$

where each j runs 0, 1, 2... and l runs 0, 1,...$2^j - 1$. Therefore, the WFCs $\tilde{\epsilon}_{j,l}$ can be used as the variables of the field δT_b. The $\tilde{\epsilon}_{j,l}$ are the fluctuations around scales $k = 2\pi n/L$ with $n = 2^j$ and at the physical area l with size $\Delta x = L/2^j$.

4.2. One-point distributions of $\delta T_{b,(j,l)}$ and $\widetilde{\delta T}_{b(j,l)}$

We plot in Figure 7 the one-point distributions of $\delta T_{b,(j,l)}$ for two temperature models $(T_0, \eta, z) = (1.3 \times 10^4 K, 2, 7)$ and $(0.8 \times 10^4 K, 2, 10)$. The scales j are taken to be 6, 8 and 10, respectively, corresponding to comoving smoothing sizes 0.78, 0.20, and 0.05 h^{-1} Mpc or angular resolutions $0'.44$, $0'.11$, and $0'.028$ at z=7, or $0'.41$, $0'.10$, and $0'.025$ at z=10. All the PDFs in Figure 7 seem to have similar shapes. A peak at $\delta T_b \simeq 0$ is given by the low mass density $(0 < \rho < 2)$ areas; Figure 6 shows that the areas with mass density $0 < \rho < 2$ do not contribute to δT_b. Except for the peaks, the PDFs of Figure 7 are flat in the range $\delta T_{b,(j,l)} < 1$ mK, and approximately of a power law at $\delta T_{b,(j,l)} > 1$ mK. The long tail obviously is given by the spikes in the δT_b field (Fig. 5). The power law tail shows a slightly smoothing scale dependence.

We plot in Figure 8 the PDFs of the WFCs, in which $\tilde{\epsilon}_{j,l}$ is replaced by $\widetilde{\delta T}_{b(j,l)} = (2^j/L)^{1/2}\tilde{\epsilon}_{j,l}$ since the latter has the dimension of temperature. The parameters used in Figure 8 are the same as those in Figure 7. The PDFs shown in Figure 8 are also weakly dependent on the temperature parameters, but the tails of the PDFs are more significantly dependent on scale j than in Figure 7. If we describe the tail by a power law $\propto \widetilde{\delta T}^{-a}_{b(j,l)}$, the index a is bigger with larger scales. In other words, the tails are longer for smaller scales. This leads to the mean power $\langle \widetilde{\delta T}^2_{b(j,l)} \rangle$ being lower for higher j (see next subsection on power spectrum).

In either Figures 7 or 8, the mean of $\delta T_{b,(j,l)}$ or $\widetilde{\delta T}_{b(j,l)}$ is given by the events corresponding to the long tail of the PDFs. That is, the maps of δT_b or $\widetilde{\delta T}_{b(j,l)}$ are very different from the Gaussian noise field.

4.3. Second-order correlations

The two-mode correlation of the SFCs $\langle \delta T_{b,(j,l)} \delta T_{b,(j,l')} \rangle$ is similar to the ordinary two-point correlation function. Figure 9 presents the correlation function $\langle \delta T_{b,(j,l)} \delta T_{b,(j,l')} \rangle$ for parameters $(T_0, \eta, z) = (1.3 \times 10^4$ K, 2, 7) with smoothing scales j = 12, 10 and 8, which correspond, respectively, to comoving sizes 0.03, 0.05, and 0.20 h^{-1} Mpc, or $0'.007$, $0'.028$ and $0'.11$. The two-mode correlation functions are typically of power law $\langle \delta T_{b,(j,l)} \delta T_{b,(j,l')} \rangle \propto r^{-\gamma}$

in the range $0.2 < r < 1$ h^{-1} Mpc with index $\gamma \simeq 0.6$. The central part of the correlation function, or $r < 0.2$ h^{-1} Mpc, is flat because of the Jeans length smoothing. The tail, or $r > 2$ h^{-1} Mpc, of the correlation function approaches $\langle \delta T_{b,(j,l)} \delta T_{b,(j,l')} \rangle = \langle \delta T_{b,(j,l)} \rangle^2 = \langle \delta T_b \rangle^2$, which is the mean of δT_b.

The two-mode correlation function of the WFCs $\langle \tilde{\epsilon}_{j,l} \tilde{\epsilon}_{j,l'} \rangle$, or $\langle \widetilde{\delta T}_{b,(j,l)} \widetilde{\delta T}_{b,(j,l')} \rangle$, generally is diagonal with respect to (l, l'), especially if the initial mass perturbation is Gaussian (Feng & Fang 2004; Guo et al. 2004). Thus we have in general

$$\langle \widetilde{\delta T}_{b,(j,l)} \widetilde{\delta T}_{b,(j,l')} \rangle = P_j \delta^K_{l,l'}, \tag{23}$$

where P_j is the DWT power spectrum of the one-dimensional field, of which the relation with the Fourier power spectrum $P(k)$ has been given in Fang & Feng (2000). Figure 10 gives the power spectrum P_j for parameters $(T_0, \eta, z) = (1.3 \times 10^4$ K, 2, 7) and $(0.8 \times 10^4$ K, 2, 10). The power spectra of these two cases are similar. However, if using angular scales, they are different. For instance, although both spectra are peaked at $j = 7$, they correspond to angular scale $0'.22$ at $z = 7$, or $0'.20$ at $z = 10$.

The power $\langle \widetilde{\delta T}^2_{b,(j,l)} \rangle$ increases from $j = 2$ (comoving scale 12.5 h^{-1} Mpc) to $j = 7$ (0.39 h^{-1} Mpc). This is because the clustering is stronger on small scales. The power $\langle \widetilde{\delta T}^2_{b,(j,l)} \rangle$ gradually decreases with j when $j > 7$ (comoving scale less than 0.39 h^{-1} Mpc), this is because of the Jeans smoothing of hydrogen gas.

4.4. High-order moments of δT_b field

High-order moments are sensitive to non-Gaussianity. We use two standard high-order moment statistics: (1) $\langle (\delta T_b - \langle \delta T_b \rangle)^{2n} \rangle^{1/n} / \langle (\delta T_b - \langle \delta T_b \rangle)^2 \rangle$ and (2) $\langle (\delta T^n_{b,j} \rangle^{1/n} / \langle (\delta T_b) \rangle$. If the δT_b field is Gaussian, the high-order moment of δT_b satisfies the relation

$$\frac{\langle (\delta T_b - \langle \delta T_b \rangle)^{2n} \rangle^{1/n}}{\langle (\delta T_b - \langle \delta T_b \rangle)^2 \rangle} = [(2n-1)!!]^{1/n}. \tag{24}$$

On the other hand, if the δT_b field is lognormal, we have

$$\frac{\langle (\delta T_b)^n \rangle^{1/n}}{\langle \delta T_b \rangle} = \exp[(1/2)(n-1)\sigma^2], \tag{25}$$

where σ is the variance of $\ln(\delta T_b)$.

We plot in Figure 11 the high-order moments $\langle (\delta T_b - \langle \delta T_b \rangle)^{2n} \rangle^{1/n} / \langle (\delta T_b - \langle \delta T_b \rangle)^2 \rangle$ and $\langle (\delta T^n_{b,j} \rangle^{1/n} / \langle (\delta T_b) \rangle$ for the parameters $(T_0, \eta, z) = (1.3 \times 10^4 K, 2, 7)$ and $(0.8 \times 10^4 K, 2, 10)$.

As a comparison, we also plot the corresponding Gaussian and LN moments in Figures 11a and 11b, respectively. Figure 11 shows that the δT_b field is neither Gaussian nor lognormal. The high-order moments are always significantly higher than a Gaussian field for $n > 1$, but always less than an LN field. In both temperature models, the two high-order moments are always quickly increasing with n when $n \leq 5$, and then slowly increasing when $n > 5$. Therefore, the non-Gaussianity of the δT_b field is less than the mass density field of hydrogen clouds. This is because high-density areas correspond to lower f_{HI} regions. The non-Gaussianity is weakened when transferring the mass field to the f_{HI} field by equation (11). Moreover, equation (12) leads to further weakening of the non-Gaussianity given by high-density peaks. Therefore, although its PDFs (Fig. 7) are long tailed, the non-Gaussianity of the δT_b field is not as strong as that of an LN field.

High-order moments are more sensitive to the tails of δT_b PDFs, and therefore, the statistics $\langle(\delta T_b - \langle\delta T_b\rangle)^{2n}\rangle^{1/n}/\langle(\delta T_b - \langle\delta T_b\rangle)^2\rangle$ and $\langle(\delta T_{b,j}^n\rangle^{1/n}/\langle(\delta T_b)\rangle$ are less dependent on the lower limit of observable δT_b. If we use only the observable events with $\delta T_b \geq 1$ mK, the high-order moments given by the truncated PDFs [Fig. 7] will not be changed very much. Moreover, the statistics $\langle(\delta T_b - \langle\delta T_b\rangle)^{2n}\rangle^{1/n}/\langle(\delta T_b - \langle\delta T_b\rangle)^2\rangle$ and $\langle(\delta T_{b,j}^n\rangle^{1/n}/\langle(\delta T_b)\rangle$ are defined by ratios of δT_b. Hence, they are less dependent on mean f_{HI}. The statistical behavior shown in Figure 11 is weakly dependent on ionizing photon parameter J in equation (11).

4.5. Scale-scale correlations of the WFCs

The so-called scale-scale correlations of a random field measures the correlation between the fluctuations on different scales (Pando et al. 1998). For δT_b field, this statistics is defined as

$$C_j^{p,p} = \frac{\langle \tilde{\epsilon}^p_{j,[l/2]} \tilde{\epsilon}^p_{j+1,l} \rangle}{\langle \tilde{\epsilon}^p_{j,[l/2]} \rangle \langle \tilde{\epsilon}^p_{j+1,l} \rangle}, \tag{26}$$

where p is an even integer. The notation [...] in equation (26) denotes the integer part of the quantity. Because the spatial range of the cell $(j,[l/2])$ is the same as that of the two cells $(j+1,l)$ and $(j+1,l+1)$, $C_j^{p,p}$ measures the correlation between the fluctuations on scales j and $j+1$ at the *same* physical area. For Gaussian noise, the variables $\tilde{\epsilon}_{j,l}$ on scales j and $j+1$ are uncorrelated, and hence we have $\langle \tilde{\epsilon}^p_{j,[l/2]} \tilde{\epsilon}^p_{j+1,l} \rangle = \langle \tilde{\epsilon}^p_{\mathbf{j,[l/2]}} \rangle \langle \tilde{\epsilon}^p_{\mathbf{j+1,l}} \rangle$, or $C^{p,p}_{\mathbf{j,j+1}} = 1$. Therefore, the scale-scale correlation is effective for drawing a non-Gaussian signal from a Gaussian background, even when the variance of the noise is comparable to the signal (Feng et al. 2000; Feng & Fang 2000).

Figure 12 presents the $C_j^{p,p}$ versus j of the δT_b field with parameters $(T_0, \eta, z) = (1.3 \times$

$10^4K, 2, 7)$ and $(0.8 \times 10^4K, 2, 10)$ and $p = 2$, 4 and 8. Figure 12 shows once again that the statistical results are less dependent on the temperature parameters considered. For all cases of $p = 2$, 4 and 8, the δT_b fields are substantially scale-scale correlated on scales $j > 3$, corresponding to length scale 6.25 h^{-1} Mpc and angular scale $3'.52$ at $z = 7$ or $3'.28$ at $z = 10$. At scale $j = 8$, or 0.20 h^{-1}Mpc, $C_j^{p,p}$ is as large as 10^2, which would be very useful for distinguishing the signal of $\delta T_b(z_0)$ from noise.

From Figure 12 we see that the scale-scale correlation is remarkably increasing from $p = 2$ to $p = 4$, but not so from $p = 4$ to $p = 8$. This is again because the PDFs of δT_b are long tailed, but not very long. This can strongly affect statistics of order $n \leq 5$, but not $n > 5$. We calculate also the scale-scale correlation for noise-contaminated samples. It indeed shows that the Gaussian noise can be filtered out with the scale-scale correlations.

5. Discussion and Conclusion

We have studied the brightness temperature excess δT_b of the redshifted 21 cm emission of hydrogen clouds in the epoch$z_r > z > z_{GP}$. According to the LN model, the mean temperature of hydrogen clouds does not undergo strong evolution and is generally $T_0 \simeq 10^4$ K. Therefore, the 21 cm emission from this epoch possesses some statistical features weakly dependent on the details of this epoch. They are as follows:

1. The random field of δT_b is substantially non-Gaussian. It consists of spikes with high δT_b and a low δT_b area between the spikes.

2. The mean of δT_b is $\simeq 2$ mK, and the variance $\langle(\delta T_b)^2\rangle^{1/2}$ is of the order of 10 mK on about arcminute scales, while the spikes can be as high as 40 mK.

3. The one-point distributions of either δT_b or $\widetilde{\delta T}_{b,(j,l)}$ have long tails approximately following power laws.

4. The nth-order moment of δT_b is quickly increasing with n when $n \leq 5$, and slowly when $n > 5$. It is very different from a Gaussian field and an LN field.

5. The scale-scale correlation is significant for all scales, which is effective for washing out Gaussian noise contamination.

All these results show that although the clustering of hydrogen gas is suppressed at $z < z_r$, the 21 cm emission fields are significantly non-Gaussian since z_r.

To obtain the above results, we used the fraction of neutral hydrogen HI given by the LN model (Liu et al. 2004). Actually, the evolution of the HI fraction in $z_r > z > z_{GP}$ is

not strongly constrained by the current observations. The optical depth τ_e is sensitive to z_r and the mean of the HI fraction in $z_r > z > z_{GP}$, but not to the details of the evolution of the HI fraction. Different evolution models of the HI and HII fractions can reasonably explain the observed τ_e. However, among the above results, the last two points (high-order moments and scale-scale correlations) are based on statistics given by the ratios of δT_b. They are probably less dependent on the HI or HII fractions.

We show that the non-Gaussian properties of the δT_b field comes from the non-Gaussianity of the mass field at high redshifts. For a given redshift z, the δT_b field of the redshifted 21 cm emission is dependent only on T_m at that redshift, but less sensitive to the details of the redshift evolution of T_m. On the other hand, in the epoch $z_r > z > z_{GP}$, T_m is in the range $10^3 - 10^4$ K. Therefore, the non-Gaussian features revealed in this paper may help in, or even be necessary for, unambiguously identifying the 21 cm emission from the epoch $z_r > z > z_{GP}$.

P.H. is supported by a Fellowship of the World Laboratory. L.L.F. acknowledges support from the National Science Foundation of China (NSFC) and the National Key Basic Research Science Foundation. This work is partially supported by the National Natural Science Foundation of China (10025313) and the National Key Basic Research Science Foundation of China (NKBRSF G19990752).

REFERENCES

Bi, H.G. 1993, ApJ, 405, 479

Bi, H.G., & Davidsen, A.F. 1997, ApJ, 479, 523.

Bi, H.G., Fang, L.Z., Feng, L.L., & Jing, Y.P. 2003, ApJ, 598, 1

Bi, H.G., Ge, J., & Fang, L.Z. 1995, ApJ, 452, 90

Black, J.H. 1981, MNRAS, 197, 553

Cen, R. 2003, ApJ, 591, 12

Choudhury, T., Srianand, R.,& Padmanabhan, T. 2001, ApJ, 559, 29

Ciardi, B., & Madau, P. 2003, ApJ, 596, 1

Coles, P., & Jones, B. 1991, MNRAS, 248, 1

Eisenstein, D., & Hu, W. 1999, ApJ, 511, 5

Fan, X., et al. 2002, AJ, 123, 1247

Fang, L.Z., & Feng, L.L. 2000, ApJ, 539, 5

Fang, L.Z., & Thews, R. 1998, Wavelets in Physics (Singapore: World Scientific)

Feng, L.L., Deng, Z.G., & Fang, L.Z. 2000, ApJ, 530, 53

Feng, L.L., & Fang, L.Z. 2000, ApJ, 535, 519

Feng, L.L. & Fang, L.Z. 2004, ApJ, 601, 54

Field, G.B. 1958, Proc. IRE, 46, 240

Field, G.B. 1959, ApJ, 129, 536

Furlanetto, S.R. & Loeb, A. 2002, ApJ, 579, 1

Furlanetto, S.R. & Loeb, A. 2003, ApJ, 611, 642

Furlanetto, S.R., Sokasian, A., & Hernquist, L. 2004, MNRAS, 347, 187

Guo, Y.C., Chu, Y.Q., & Fang, L.Z. 2004, ApJ, 610, 51

Haiman, Z., & Holder, G.P. 2003, ApJ, 595, 1

He, P., Feng, L.L., & Fang, L.Z. 2004, 612, 14

Holder, G., Haiman, Z., Kaplinghat, M., & Knox, L. 2003, ApJ, 595, 13

Hui, L., & Haiman, Z. 2003, ApJ, 596, 9

Iliev, I. T., Shapiro, P.R., Ferrara, A., & Martel, H. 2002, ApJ, 572, L123,

Iliev, I. T., Scannapieco, E., Martel, H., & Shapiro, P. R. 2003, MNRAS, 341, 81

Jamkhedkar, P., Feng, L.L., Zheng, W., Kirkman, D., Tytler, D., & Fang, L.Z. 2003, MNRAS, 343, 1110

Jamkhedkar, P., Zhan, H. & Fang, L.Z. 2000, ApJ, 543, L1

Jones, B.T. 1999, MNRAS, 307, 376

Kogut, A., et al. 2003, ApJS, 148, 161

Liu, J., Fang, L.Z., Feng, L.L., & Bi,H.G. 2004, ApJ, 605, 591

Morales, M.F., & Hewitt, J. 2004, in press (astro-ph/0312437)

Onken, C.A., & Miralda-Escudé, J. 2004, ApJ, 610, 1

Ostriker, J.P., & Ikeuchi, S. 1983, ApJ, 268, L63

Pando, J., Lipa, P., Greiner, M., & Fang, L.Z. 1998 ApJ, 496, 9

Pando, J., Feng, L.L., Jamkhedkar, P., Zheng, W., Kirkman, D., Tytler, D. and Fang, L.Z. 2002, ApJ, 574, 575

Peebles, P.J.E. 1993, Principles of Physical Cosmology (Princeton University Press)

Pen, U.L., Wu, X. P, & Peterson, J. 2004, preprint (astro-ph/0404083)

Szapudi, I., & Kaiser, N. 2003, ApJ, 583, L1

Theuns, T., Bernardi, M., Frieman, J., Hewett, P., Schaye, J., Sheth, R.K., & Subburao, M. 2002, ApJ, 574, L111

Tozzi, P., Madau, P., Meiksin, A., & Rees, M.J. 2000, ApJ, 528, 597

Wild, J.P. 1952, ApJ, 115, 206

Wyithe, J., & Loeb, A. 2003, ApJ, 588, L69

Zaldarriaga, M., Furlanetto, S.R., & Hernquist, L. 2004, ApJ, 608, 622

This preprint was prepared with the AAS LaTeX macros v5.2.

Fig. 1.— Comoving Jeans length x_J as a function of the cosmic scale factor $1/(1+z)$. In the period $z_r < z < z_{GP}$, the mean temperature of hydrogen is assumed to be $T_m = T_0[(1+z)/(1+z_r)]^2$, with $T_0 = 1.3 \times 10^4$ K (solid line) and $0.8{\times}10^4$ K (dotted line).

Fig. 2.— Variance σ_0 of linear perturbations as a function of $1/(1+z)$, which is calculated with the x_J given by Fig. 1.

Fig. 3.— Temperature evolution in the three epochs: (1) $z > z_r = 18$, $T = 4[(1+z)/16]^2$ K; (2) $z_r > z > z_{GP} = 7$, $T = T_0[(1+z)/(1+z_r)]^2$, with $T_0 = 1.3 \times 10^4$ K (solid line), and $0.8{\times}10^4$ K (dotted line); (3) $z < z_{GP}$, $T \simeq T_0$. The increase of T at $z = 3.3$ is due to He reionization.

Fig. 4.— Realization of hydrogen density fields at redshifts 7, 10 and 15. The densities are in units of $\bar{\rho}_{IGM}$.

Fig. 5.— Realization of the fields of T_b, τ_{21} and δT_b. The relevant parameters (T_0, η, z) are taken to be (1.3×10^4 K, 2, 7).

Fig. 6.— Cumulative $\langle \delta T_b^2 \rangle^{1/2}(> \rho)$ mK for field with density $> \rho$ as a function of ρ. The parameters (T_0, η, z) are taken to be (1.3×10^4 K, 2, 7).

Fig. 7.— One-point distributions of $\delta T_{b,(j,l)}$ for $(T_0, \eta, z) = (1.3 \times 10^4$ K, 2, 7) (left panels) and (0.8×10^4 K, 2, 10) (right panels). The smoothing scales are $j = 6$, 8, and 10.

Fig. 8.— One-point distributions of $\widetilde{\delta T}_{b,(j,l)}$ for $(T_0, \eta, z) = (1.3 \times 10^4$ K, 2, 7) (left panels) and (0.8×10^4 K, 2, 10) (right panels). The smoothing scales are $j = 6$, 8, and 10.

Fig. 9.— Two-mode correlation function $\ln\langle \delta T_{b,(j,l)} \delta T_{b,(j,l')} \rangle$ vs. $\ln r$ (h^{-1} Mpc) for parameters $(T_0, \eta, z) = (1.3 \times 10^4$ K, 2, 7). The smoothing scales are $j = 8$, 10, and 12.

Fig. 10.— DWT power spectrum P_j of the δT_b field for parameters $(T_0, \eta, z) = (1.3 \times 10^4$ K, 2, 7) and (0.8×10^4 K, 2, 10).

Fig. 11.— The n-dependence of (a) $\langle(\delta T_{b,j} - \langle \delta T_{b,j} \rangle)^{2n}\rangle^{1/n} / \langle(\delta T_{b,j} - \langle \delta T_{b,j} \rangle)^2\rangle$ and (b) $\langle(\delta T_{b,j}^n\rangle^{1/n} / \langle(\delta T_b)\rangle$ for parameters $(T_0, \eta, z) = (1.3 \times 10^4$ K, 2, 7) (left panels) and (0.8×10^4 K, 2, 10) (right panels)

Fig. 12.— Scale-scale correlation $C_j^{p,p}$ vs. j for parameters $(T_0, \eta, z) = (1.3 \times 10^4$ K, 2, 7) (left panels) and (0.8×10^4 K, 2, 10) (right panels); p is taken to be 2, 4, and 8.

This figure "fig2.jpg" is available in "jpg" format from:

http://arXiv.org/ps/astro-ph/0406544v2

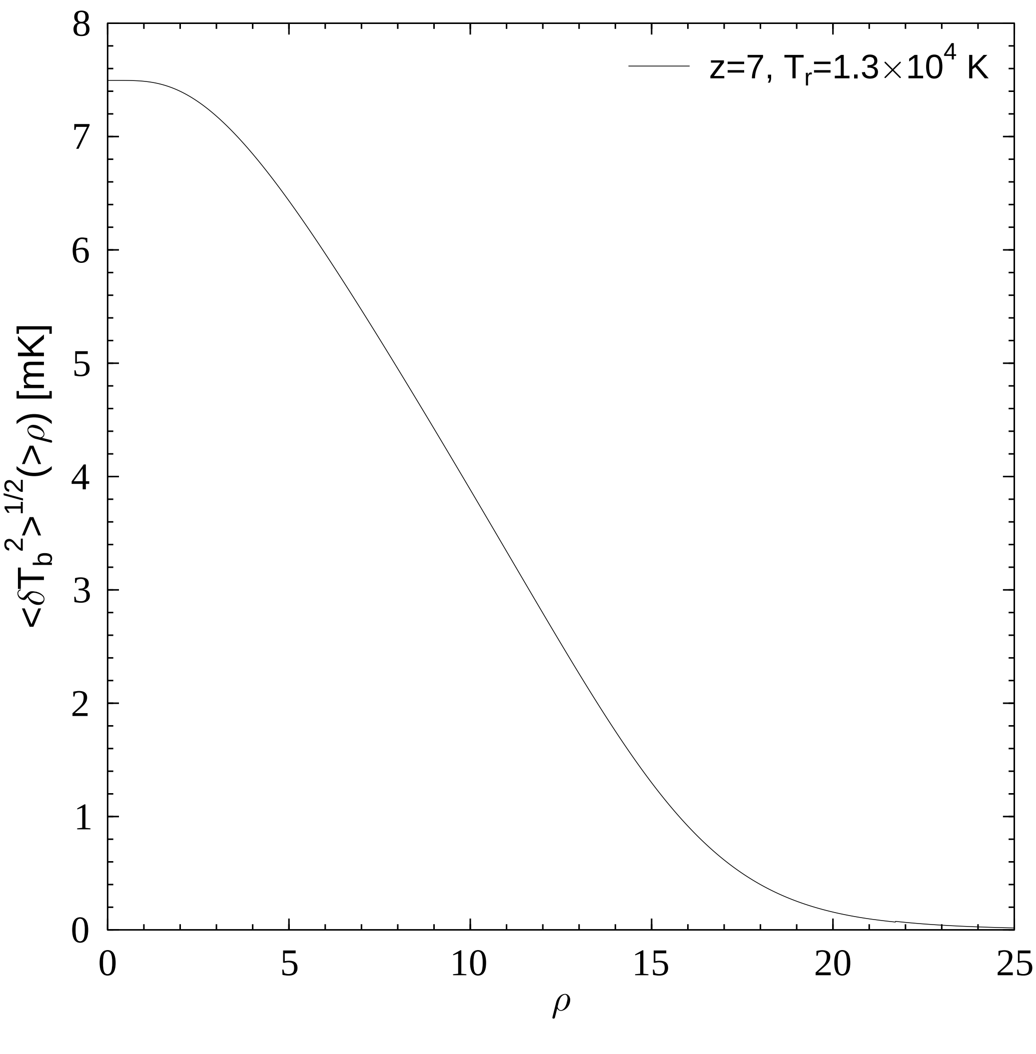

z=7, T$_r$=1.3×10^4 K
<δT$_b$^{2}>$^{1/2}$(>ρ) [mK]
ρ
0
5
10
15
20
25
1
2
3
4
5
6
7
8

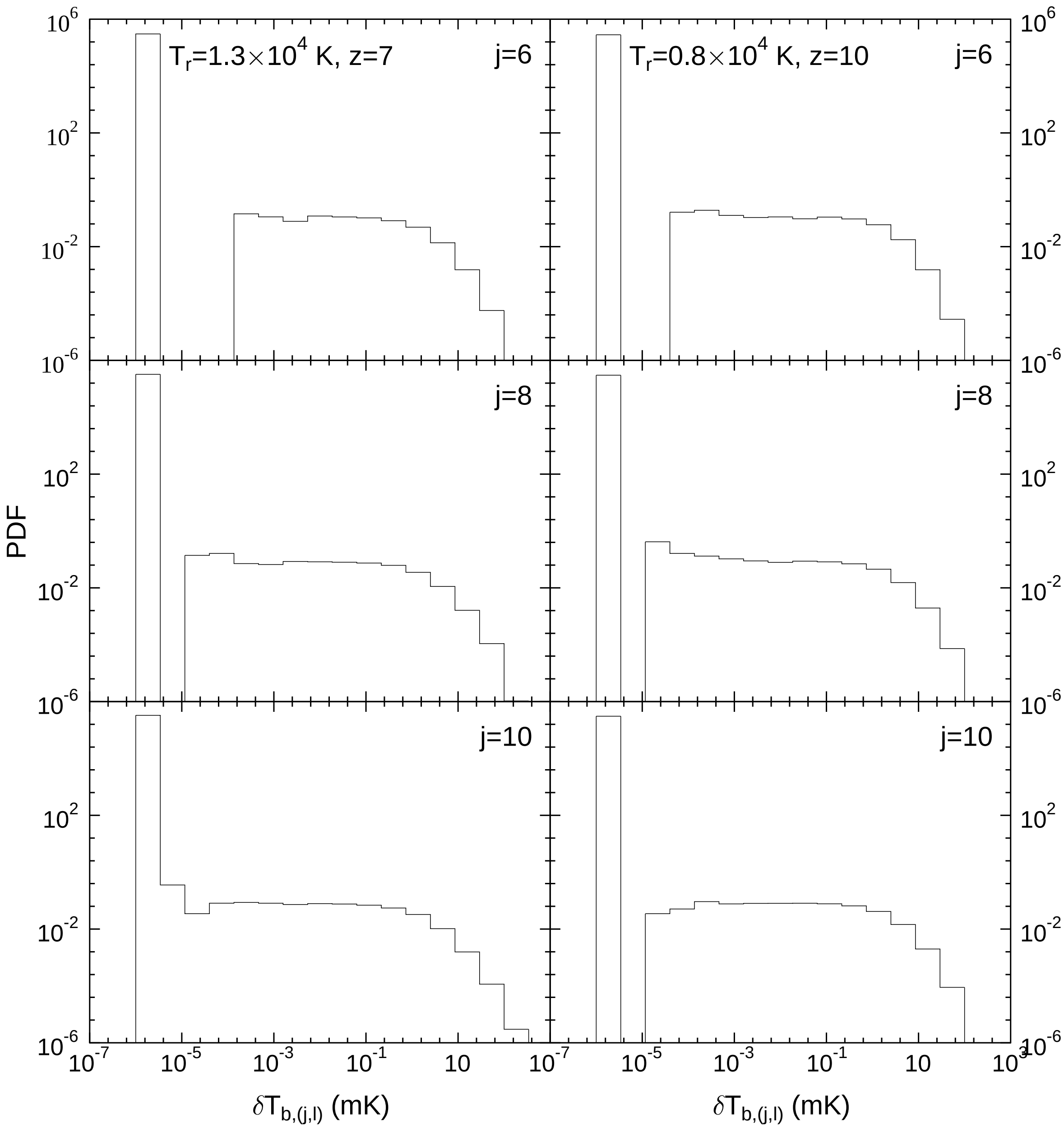

$T_r=1.3\times10^4$ K, z=7
$T_r=0.8\times10^4$ K, z=10
j=6
j=8
j=10
PDF
$\delta T_{b,(j,l)}$ (mK)

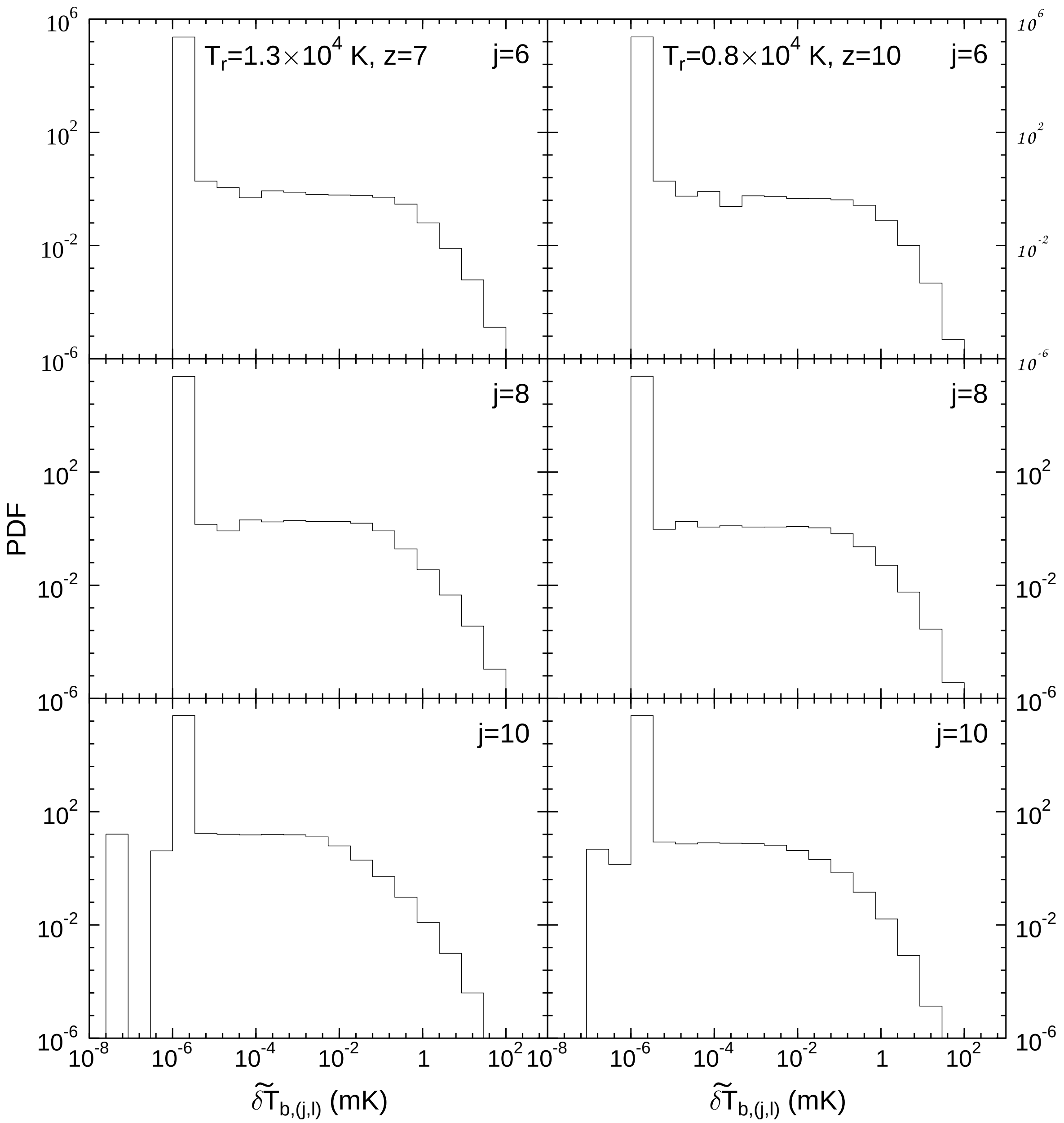

$T_r=1.3\times10^4$ K, z=7
$T_r=0.8\times10^4$ K, z=10
j=6
j=8
j=10
PDF
$\widetilde{\delta T}_{b,(j,l)}$ (mK)

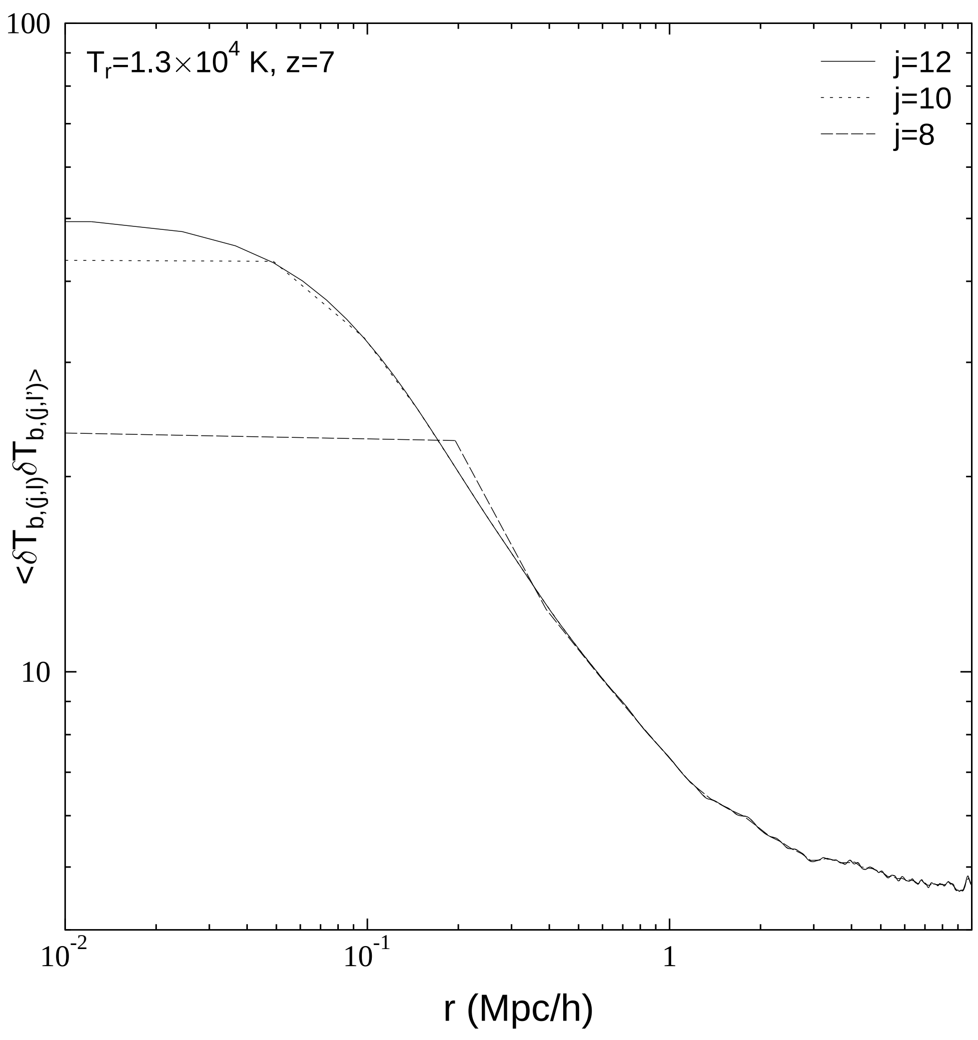

T_r=1.3×10^4 K, z=7
j=12
j=10
j=8
100
10
10^{-2}
10^{-1}
1
r (Mpc/h)
<$\delta T_{b,(j,l)}\delta T_{b,(j,l')}$>

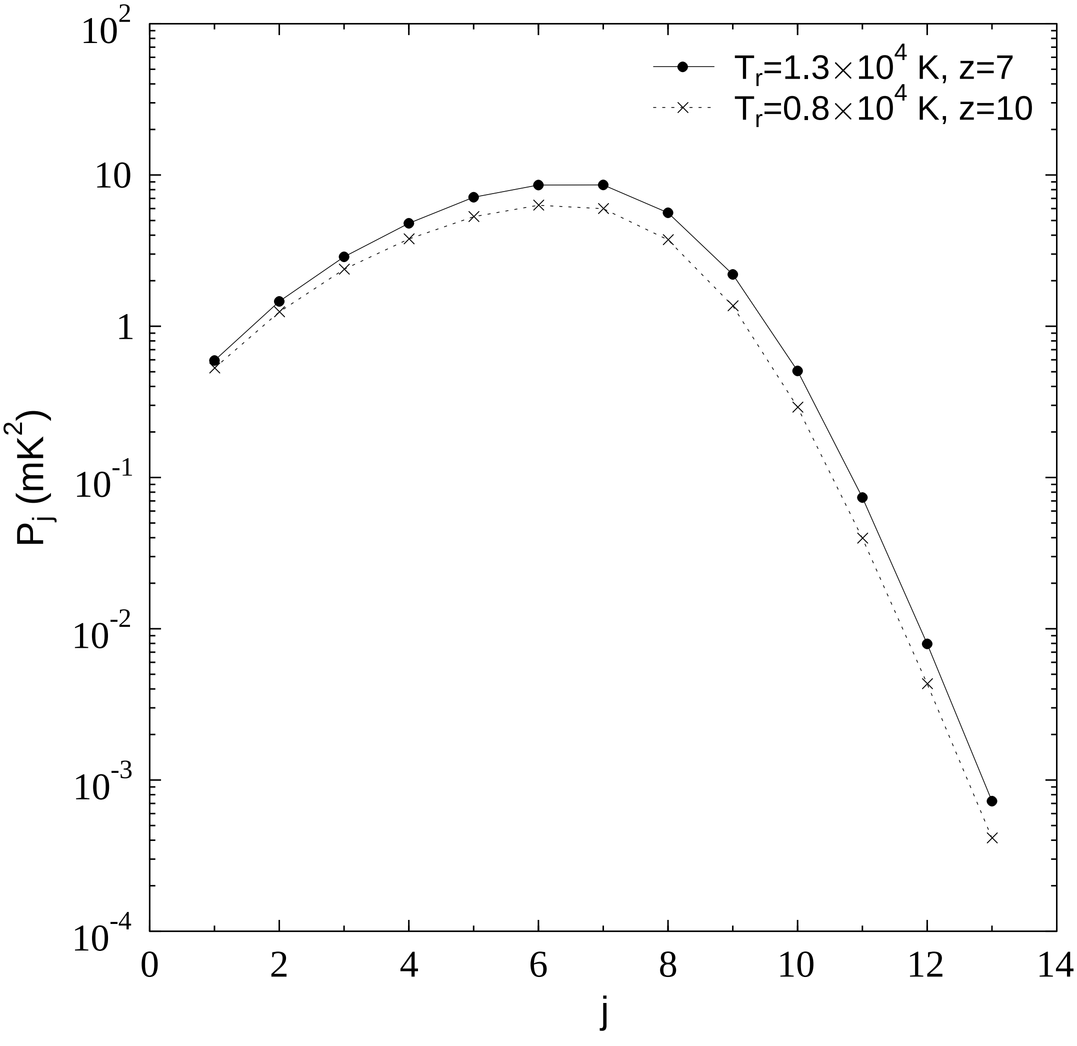

T_r=1.3×10^4 K, z=7
T_r=0.8×10^4 K, z=10
P_j (mK^2)
j
10^2
10
1
10^{-1}
10^{-2}
10^{-3}
10^{-4}
0
2
4
6
8
10
12
14

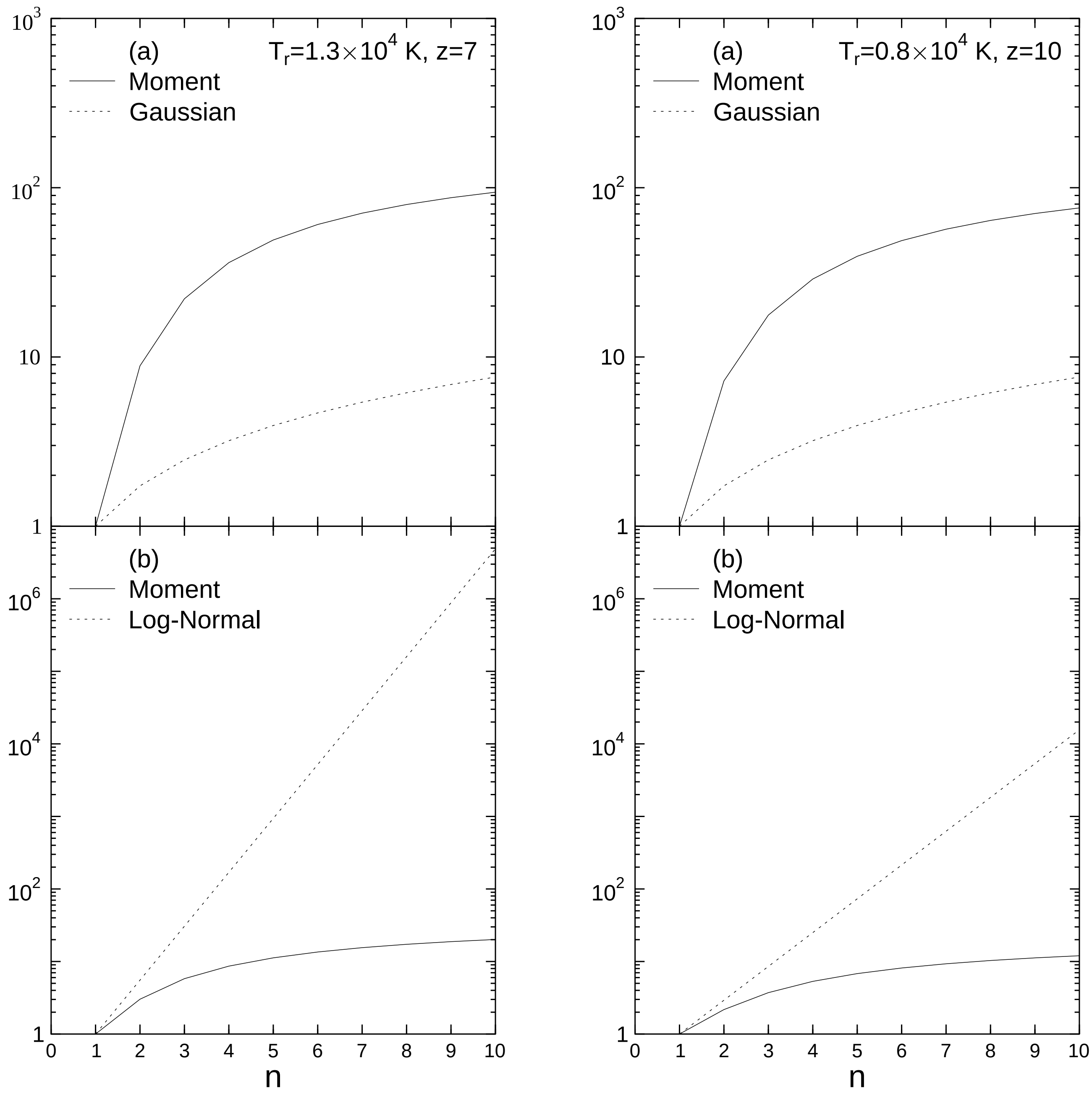

(a)
T_r=1.3×10^4 K, z=7
Moment
Gaussian
(b)
Moment
Log-Normal
(a)
T_r=0.8×10^4 K, z=10
Moment
Gaussian
(b)
Moment
Log-Normal
n
n

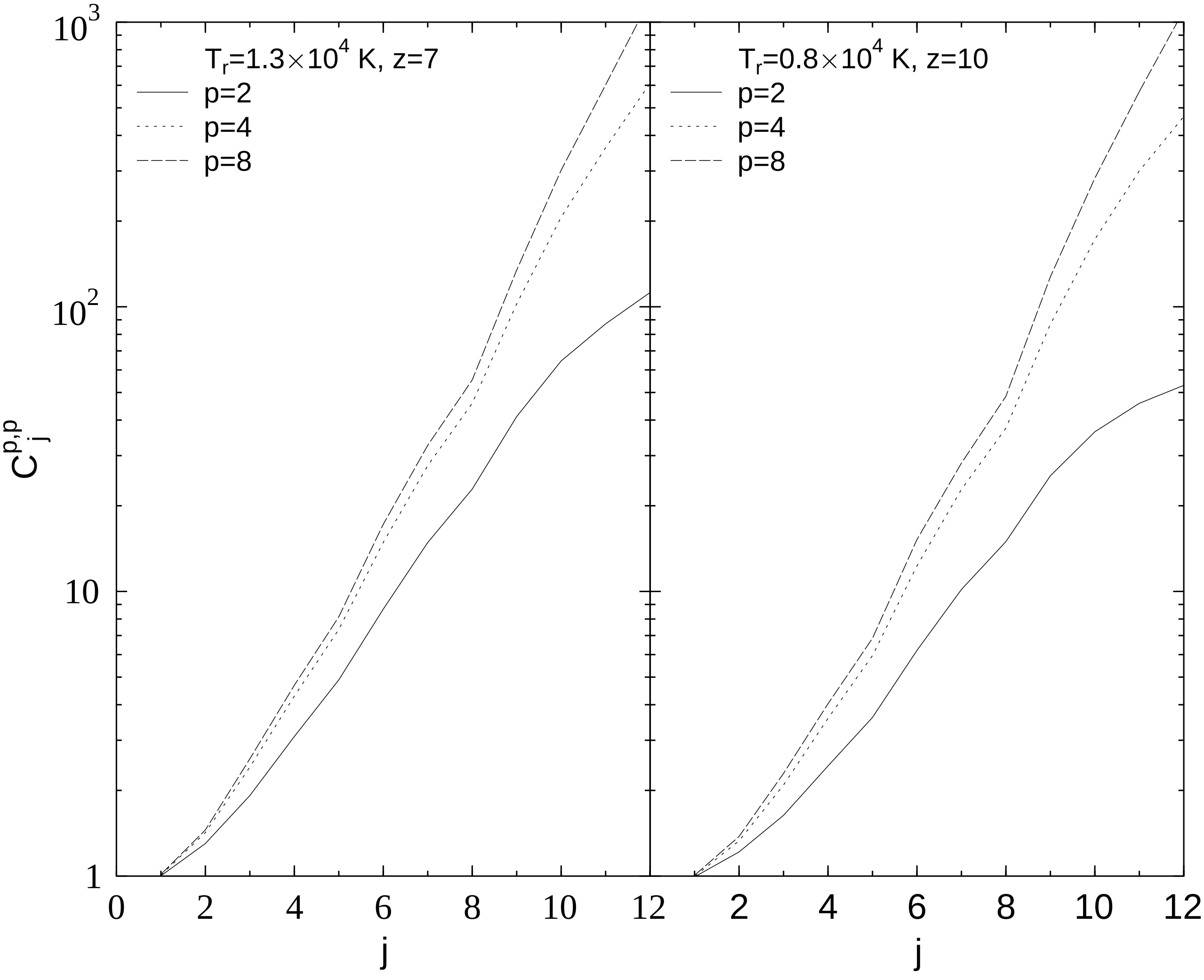

$T_r=1.3\times10^4$ K, z=7
p=2
p=4
p=8
$T_r=0.8\times10^4$ K, z=10
p=2
p=4
p=8
$C_j^{p,p}$
j
j
10^3
10^2
10
1
0
2
4
6
8
10
12